



**Radiative Properties and Line Trapping
Effects in Post-Explosion Inertial Fusion
Plasmas**

J.J. MacFarlane and P. Wang

June 1991

UWFDM-853

Phys. Fluids B 3 (1991) 3494.

FUSION TECHNOLOGY INSTITUTE

UNIVERSITY OF WISCONSIN

MADISON WISCONSIN

DISCLAIMER

This report was prepared as an account of work sponsored by an agency of the United States Government. Neither the United States Government, nor any agency thereof, nor any of their employees, makes any warranty, express or implied, or assumes any legal liability or responsibility for the accuracy, completeness, or usefulness of any information, apparatus, product, or process disclosed, or represents that its use would not infringe privately owned rights. Reference herein to any specific commercial product, process, or service by trade name, trademark, manufacturer, or otherwise, does not necessarily constitute or imply its endorsement, recommendation, or favoring by the United States Government or any agency thereof. The views and opinions of authors expressed herein do not necessarily state or reflect those of the United States Government or any agency thereof.

**Radiative Properties and Line Trapping Effects
in Post-Explosion Inertial Fusion Plasmas**

J.J. MacFarlane and P. Wang

Fusion Technology Institute
University of Wisconsin
1500 Engineering Drive
Madison, WI 53706

<http://fti.neep.wisc.edu>

June 1991

UWFDM-853

**Radiative Properties and Line Trapping Effects in
Post-Explosion Inertial Fusion Plasmas**

J.J. MacFarlane and P. Wang

Fusion Technology Institute
Nuclear Engineering and Engineering Physics Department
University of Wisconsin-Madison
1500 Johnson Drive
Madison WI 53706

June 1991

UWFDM-853

To be published in *Physics of Fluids*.

Abstract

Radiative transfer will play a major role in energy transport within post-explosion inertial confinement fusion (ICF) plasmas. The physical processes affecting radiative energy transport in such moderate-density plasmas are qualitatively different from those of many higher-opacity laboratory plasmas, and reliable analyses of their radiative properties require the use of relatively detailed physical models. In this paper, we investigate the radiative processes of plasmas generated by high-gain inertial fusion pellet explosions. We use a non-LTE radiative transfer/ionization balance code in which steady-state ionization and excitation populations are calculated by solving multilevel atomic rate equations self-consistently with the radiation field. We show that for much of their hydrodynamic evolution these plasmas are often optically thick to line radiation, but optically thin to the bulk of the continuum radiation. Because of this, line trapping — i.e., the self-attenuation of line radiation in their optically thick cores — plays a critical role in both altering the atomic level populations and in significantly reducing the escaping radiation flux. We compare our results with those obtained using thermal equilibrium, LTE, optically thin, and multigroup radiation diffusion models. We also discuss the ramifications of our results for radiation-induced damage in high-gain ICF facilities.

1. Introduction

Radiation energy transport plays a crucial role in many present-day high energy density laboratory plasma experiments. Examples include gas puff Z-pinch experiments for x-ray generation,^{1,2} hydrogen Z-pinch plasmas created to study the interaction of heavy ion beams with high-temperature matter,^{3,4} and laser and ion beam-generated plasma expansions.^{5–8} It is important to understand the radiative properties of such plasmas for at least two reasons. First, the exchange of energy between the plasma and the radiation field affects the dynamics of the bulk plasma motion. And second, reliable interpretation of spectroscopic

data in diagnosing plasma temperatures and densities often requires a good quantitative understanding of plasma opacity effects.

In this paper, we investigate the radiative properties of plasmas created as a result of high-gain inertial confinement fusion (ICF) target explosions. Such plasmas are created immediately following the sudden release of energy from a DT-filled target ignited by either high-intensity laser or ion beams. The transport of radiation in such plasmas, as well as those mentioned in the preceding paragraph, is qualitatively different from that in relatively high opacity plasmas, such as the interior regions of ICF pellets and those resulting from large-scale weapons explosions. The difference results from the fact that the former are optically thin to continuum radiation at most photon energies, and the atomic level populations are not in local thermodynamic equilibrium (LTE).

It is expected that the energy released in high-gain ICF target explosions will be $\sim 10^2 - 10^3$ MJ ($\sim 10^{15} - 10^{16}$ ergs).⁹⁻¹³ In near-term engineering test facilities, currently envisioned to be the Laboratory Microfusion Facility (LMF),¹⁴ the shot rate is likely to be about one to a few per day. It is possible that construction of the first high-gain ICF facility will begin within the next 10 years.¹⁴ For commercial power reactors, a shot repetition rate of 2 to 10 per second is expected. Roughly one-third of the energy released in each explosion will be in the form of x-rays and high-speed target debris ions. Most of the remaining energy will be carried away by neutrons. Because the x-rays and debris ions have short mean free paths in solid materials, the specific energy of the material absorbing them can be raised substantially in a short period of time. For an unprotected wall — or for that matter, diagnostic equipment or driver components — located within several meters of the target, the x-ray and debris flux from a single target explosion can vaporize the first several microns of exposed material (equivalent to $\sim 10^3$ grams).^{13,15} In addition to problems associated with the excessive erosion rates, the high heat fluxes can also produce large thermal and mechanical stresses in the chamber first wall.^{16,17} Another important issue for

ICF reactors is whether material which is vaporized can be cleared from the path of the driver beam before the next shot.

To protect the target chamber wall, driver components, and diagnostic equipment from x-rays and debris ions, the chamber — which is typically a few meters in radius — can be filled with a moderate density “buffer” gas. The density required to stop a significant fraction of the x-ray and ion energy within the gas is $\gtrsim 10^{16}$ atoms/cm³. The energy absorbed in the buffer gas is then transported radially outward primarily by two processes: reradiated photons and hydrodynamic expansion. It is important to understand the partitioning of energy between these two processes for several reasons. If the energy is transported by radiation through the plasma too rapidly, problems can again arise from high stresses, heat fluxes, and erosion rates. On the other hand, if the time scale over which energy is reradiated to the wall exceeds the time it takes for heat to be conducted away from the thin “heat-absorbing” surface layer through the solid material, the temperature rise in the absorbing layer will be less. In this case, the problems associated with high heat fluxes are greatly reduced. However, because radiative energy losses are less, the strength of the shock generated by the expanding high temperature gas will be greater.

The purpose of this paper is to examine the radiative properties of plasmas created as a result of the rapid release of energy from high-gain ICF target explosions. Such plasmas are generally *not* in local thermodynamic equilibrium. That is, the atomic level populations are not well-described by Boltzmann statistics and the Saha equation. This is because: (1) collisional deexcitation and recombination rates are exceeded by their radiative counterparts,¹⁸ and (2) the radiation field is unable to “force” the populations into LTE because the plasmas are not optically thick at all photon energies. The radiation field of these plasmas looks nothing like a blackbody spectrum, or any smoothly varying spectrum for that matter. Rather, the radiation spectra exhibit many strong emission lines which rise far above the continuum. We will show that because the lines tend to be optically thick while the

continuum is often optically thin, the transport of *line* radiation is a critical process which affects the rate at which radiative energy escapes the plasma.

A number of earlier theoretical studies of energy transport in ICF target chambers have relied on radiation diffusion models to transport radiation.^{12,13,15,19,20} This type of model is valid when the photon mean free paths are small compared to the dimensions of the plasma.²¹ When this occurs, the total radiation flux (lines plus continuum) tends to be a smooth function of the photon energy. It is reasonable under these circumstances to group together the opacities from a large number of transitions into a relatively small number of photon energy bins ($\sim 10^1 - 10^2$). However, we will show below that because the mean free paths in target chamber plasmas are not small at all photon energies, multigroup radiation diffusion models using a reasonable number of energy groups can significantly overestimate the radiation flux escaping these plasmas. We will also show that simple plasma models based on either thermal equilibrium or optically thin approximations are grossly inadequate in characterizing the radiation field.

Below, we present a series of non-LTE radiative transfer calculations for plasmas with conditions typical of those expected for the post-explosion environment within ICF target chambers. Specifically, we have calculated the radiative properties of spherical plasmas with uniform temperature and density to examine the extent to which radiation trapping in line cores reduces the escaping flux. We examine the effects of photoexcitation on the atomic level populations, and present results for detailed emission spectra. To study this, we used a radiation transfer/ionization balance code in which atomic level populations are determined by the self-consistent solution of radiative transfer and multilevel atomic rate equations. Atomic rate coefficients for the various ionization and excitation transitions were calculated using a combination of Hartree-Fock, semi-classical impact parameter, and distorted wave models.

2. Theoretical Models

We present in this section a brief overview of the theoretical models used to compute the radiative properties of moderate-density inertial fusion plasmas. A detailed description of these models is presented elsewhere.^{22–25}

2.1. Non-LTE Radiation Transport and Ionization Balance

Steady-state ionization and excitation populations are computed by solving multilevel atomic rate equations self-consistently with the radiation field. This is a collisional-radiative equilibrium (CRE) model which includes the effects of photoexcitation and photoionization on the atomic level populations. Detailed configuration accounting (DCA) is employed to track the level populations; that is, the population of each atomic level is determined from the collisional and radiative transition rates between each level. The steady-state rate equation for atomic level i can be written as:

$$\frac{dn_i}{dt} = -n_i \sum_{j \neq i}^{N_L} W_{ij} + \sum_{j \neq i}^{N_L} n_j W_{ji} = 0, \quad (1)$$

where W_{ij} and W_{ji} are the depopulating and populating rates between levels i and j , n_i is the number density of level i , and N_L represents the total number of levels in the system. For upward transitions ($i < j$):

$$W_{ij} = B_{ij} \bar{J}_{ij} + n_e C_{ij} + n_e \gamma_{ij} + \mathcal{R}_{ij}, \quad (2)$$

while for downward transitions ($i > j$):

$$W_{ij} = A_{ij} + B'_{ij} \bar{J}_{ij} + n_e D_{ij} + n_e \alpha_{ij} + \mathcal{R}'_{ij} + n_e^2 \delta_{ij}, \quad (3)$$

where n_e is the electron density, $\bar{J}_{ij} \equiv \int \phi_{ij}(\nu) J_\nu d\nu$ is the cross section-weighted mean intensity for bound-bound transitions, and $\phi_{ij}(\nu)$ is the line profile. The rate coefficients for the various terms are: spontaneous emission (A_{ij}), stimulated absorption (B_{ij}) and emission (B'_{ij}), collisional excitation (C_{ij}), collisional deexcitation (D_{ij}), radiative plus dielectronic recombination (α_{ij}), collisional ionization (γ_{ij}), collisional recombination (δ_{ij}), photoabsorption (\mathcal{R}_{ij}), and stimulated recombinations (\mathcal{R}'_{ij}).

The photoexcitation and photoionization rates depend on the characteristics of the radiation field. To evaluate these rates we use an escape probability radiation transport model.^{22,26,27} In this approach, the stimulated absorption and emission rates are written in terms of zone-to-zone coupling coefficients, Q^{ea} , so that:

$$n_j^a B_{ji} \bar{J}_{ij} - n_i^a B_{ij} \bar{J}_{ij} = \begin{cases} -A_{ji} \sum_{e=1}^{N_D} n_j^e Q_{ji}^{ea}, & (i < j) \\ A_{ij} \sum_{e=1}^{N_D} n_i^e Q_{ij}^{ea}, & (i > j). \end{cases} \quad (4)$$

The quantity Q_{ij}^{ea} represents the probability a photon emitted in zone e from the transition $i \rightarrow j$ is absorbed in zone a . The Q^{ea} 's for each transition are determined using frequency-averaged escape probability integrals which are evaluated along a single mean scattering angle. This approach has been shown to lead to computationally efficient solutions with only a modest loss in accuracy.

2.2. Atomic Model

In our atomic model, every state of an ion is coupled to the ground state of the next higher ionization stage by collisional ionization and recombination, photoionization and stimulated recombination, and radiative recombination. In addition, the ground states of adjacent ions are coupled by dielectronic recombination. For He-like and Li-like ions the level coupling is complete; thus, each excited state of these ions is coupled to all other excited states of the ion and the ground state. For other ions, only electric dipole allowed transitions are considered. A schematic illustration of the transitions considered in our model is shown in Figure 1 for the simple case of a 3-level atom.

Atomic data have been obtained using a suite of atomic physics codes.²⁵ Single configuration Hartree-Fock calculations were performed to determine energy levels, oscillator strengths, and photoionization cross sections. The accuracy of the radiative data is expected to be better than 20 percent. Although more accurate data could be obtained using the multiconfiguration Hartree-Fock option, we are not concerned with detailed spectral analyses in this paper. Collisional strengths were calculated using a combination of distorted wave,²⁸

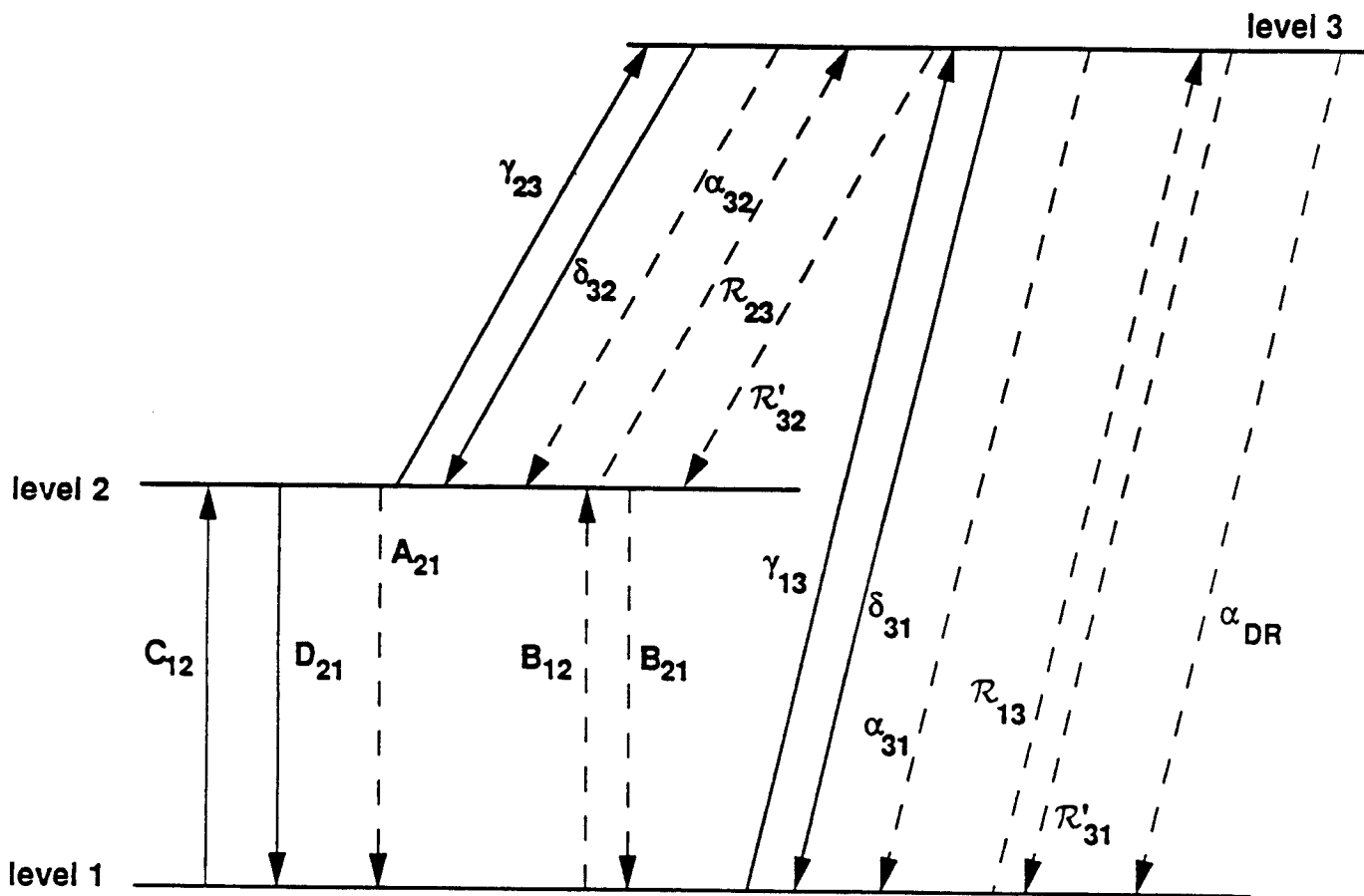


Figure 1. Schematic illustration of the transitions for a 3-level atom.

Born-Oppenheimer, and semi-classical models.²⁹ For the important resonance transitions from the ground state to the higher levels, the distorted wave model was used. For less important transitions, the latter two models were employed. Dielectronic recombination rates were computed using the Burgess-Mertz model³⁰ in conjunction with Hartree-Fock energies and oscillator strengths.

Roughly 10 energy levels were used to model each of the most abundant ions in each calculation. A typical energy level diagram is shown in Figure 2 for Ar VII. An L-S coupling scheme is used for the atomic level structure. Also shown are the energies of each level relative to fully ionized Ar and the ground state energy of Ar VII.

2.3. Spectral Flux Calculation

To compute the opacities and optical depths in each spatial zone, we consider the contributions from free-free, bound-free, and bound-bound transitions. The opacity can be written as:²¹

$$\begin{aligned} \chi_\nu = & \sum_j n_e n_{j+1} (1 - e^{h\nu/kT}) \alpha^{ff}(\nu) \\ & + \sum_j \sum_n [n_{nj} - n_{nj}^* e^{-h\nu/kT}] \alpha_n^{bf}(\nu) \\ & + \sum_j \sum_n \sum_{m>n} \left[n_{nj} - \left(\frac{g_{nj}}{g_{mj}} \right) n_{mj} \right] \alpha_{mn}^{bb}(\nu), \end{aligned} \quad (5)$$

where the index j refers to the ionization stage, n and m refer to the excitation levels, n_e is the electron density, g_{nj} and g_{mj} are the statistical weights, n_{nj} is the number density of atoms in level n of ionization stage j , and n_{j+1} is the number density of atoms in ionization stage $j + 1$ summed over all excitation levels. The quantity n_{nj}^* is the LTE population of state n_{nj} computed using the actual ion density of the upper ionization stage. The first term in Eq. (5) is the contribution from free-free absorption, the second is from bound-free absorption, and the third is due to bound-bound absorption. The free-free cross section is













Configuration	Term		$E^*(2\text{Ry})$	$E^{**}(\text{eV})$
$1s^2 2s^2 2p^6 3s^1$	$2s$		-512.0704	122.07
$1s^2 2s^2 2p^6 3s^1 4d^1$	1D		-513.7101	77.45
	3D		-513.7265	77.00
$1s^2 2s^2 2p^6 3s^1 4p^1$	1P		-514.0020	69.50
	3P		-514.0338	68.63
$1s^2 2s^2 2p^6 3s^1 4s^1$	1S		-514.2662	62.31
	3S		-514.2758	62.05
$1s^2 2s^2 2p^6 3s^1 3d^1$	1D		-515.0007	42.34
	3D		-515.1383	38.58
$1s^2 2s^2 2p^6 3s^1 3p^1$	1P		-515.7668	21.48
	3P		-516.0971	12.49
$1s^2 2s^2 2p^6 3s^2$	$1s$		-516.5562	0.0

Figure 2. Energy level diagram for Ar VII. The energies are shown for two scales: one in atomic units (1 a.u. = 2 Ry = 27.2 eV) measured relative to fully ionized Ar (E^*); the other in eV measured relative to the ground state of Ar VII (E^{**}).

given by

$$\alpha^{ff}(\nu) = \left(\frac{4e^6}{3ch} \right) \left(\frac{3\pi}{3km_e} \right)^{1/2} \overline{g_{ff}} Z_{eff}^2 T^{-1/2} \nu^{-3}, \quad (6)$$

where e and m_e are the electron charge and mass, respectively, c is the speed of light, h is Planck's constant, k is Boltzmann's constant, $\overline{g_{ff}}$ is the free-free Gaunt factor, and Z_{eff} is the effective charge.

In the calculations discussed below, we use a hydrogenic frequency dependence for the bound-free absorption cross section:

$$\alpha^{bf}(\nu) = \alpha^{bf}(\nu_1) \left(\frac{\nu_1}{\nu} \right)^3, \quad \nu \geq \nu_1, \quad (7)$$

where ν_1 is the cutoff frequency. The value of $\alpha^{bf}(\nu_1)$ is determined such that it is consistent with the radiative recombination rate, which is based on Hartree-Fock calculations. The bound-bound cross section is given by

$$\alpha^{bb}(\nu) = \left(\frac{\pi e^2}{m_e c} \right) f_{nm} \phi_\nu, \quad (8)$$

where f_{nm} is the oscillator strength and ϕ_ν is the normalized line profile ($\int \phi_\nu d\nu = 1$). A Doppler profile is assumed.

The flux at the surface due to photons emitted in zone d , $F_{\nu,d}$, can be written in terms of the plasma emissivity of the zone, $\eta_{\nu,d}$:

$$F_{\nu,d} = \frac{4\pi\eta_{\nu,d}\Delta V_d}{A} \mathcal{A}_{\nu,d}, \quad (9)$$

where ΔV_d is the volume of zone d , and A is the area of the plasma boundary. The attenuation factor, $\mathcal{A}_{\nu,d}$, represents the attenuation due to all other zones along the path to the boundary. The emissivity can be written as:²¹

$$\begin{aligned} \eta_\nu = & \left(\frac{2h\nu^3}{c^2} \right) \sum_j \left\{ n_e n_{j+1} e^{-h\nu/kT} \alpha^{ff}(\nu) \right. \\ & + \sum_n n_{nj}^* e^{-h\nu/kT} \alpha_n^{bf}(\nu) \\ & \left. + \sum_n \sum_{m>n} \left(\frac{g_{nj}}{g_{mj}} \right) n_{mj} \alpha_{mn}^{bb}(\nu) \right\}. \end{aligned} \quad (10)$$

The optical depths for each zone are computed along a path defined by the mean scattering angle. The attenuation factor is obtained by averaging $e^{-\tau_\nu}$ over the emitting zone:

$$\mathcal{A}_{\nu,d} = \frac{1}{\Delta\tau_{\nu,d}} \int_{\tau_{\nu,d}}^{\tau_{\nu,d} + \Delta\tau_{\nu,d}} e^{-\tau_\nu} d\tau_\nu, \quad (11)$$

where $\tau_{\nu,d}$ is the optical depth from the plasma surface to the nearer boundary of the emitting zone. In a typical calculation, the flux is computed at $\sim 10^3$ frequency points.

3. Results

For our study, we have selected a range of plasma parameters consistent with those expected for the environment surrounding an inertial fusion target explosion. We consider spherical argon plasmas of uniform temperature and density. The density selected for the majority of our calculations is $n = 3 \times 10^{16}$ atoms/cm³. This corresponds to a gas pressure of about 1 Torr (= 0.00133 bar) at room temperature. At this density, a majority of the target x-ray and debris ion energy can be absorbed within a few meters.^{12,13,15} The temperatures and radii of the plasma were chosen to represent snapshots in time of an expanding, cooling plasma: $R = 0.3$ m at $T = 1$ keV, $R = 1$ m at $T = 30$ eV, and $R = 4$ m at $T = 2$ eV (1 eV = 11,605 K). For these conditions, $\sim 10^2$ MJ of internal energy is contained in the hot plasma.

In each calculation, we computed populations for approximately 40 atomic levels distributed over the 4 or 5 most populated ionization stages. Typically, 7 to 11 of the lowest lying energy levels were chosen for each ion.

3.1. Effects of Photoexcitation

Let us first examine the effects of photoexcitation on the population distributions. For plasmas in which all reaction rates are dominated by collisional transitions, the populations are in LTE and are therefore specified by the Saha equation and Boltzmann statistics.³¹ However, for the plasma conditions of interest the rates of radiative recombination and spontaneous radiative decay often exceed their collisional counterparts.¹⁸ The effect of this

is to decrease both the mean ionization stage and the populations of the excited states. The effect of the radiation field on the populations is to “pump” the states back in the direction of their LTE values. Thus, in plasma regions which are very much “optically thick” to an exciting photon, the relative populations of upper and lower levels again approach LTE — even when collisional rates are low. However, near the “boundary” of the plasma (i.e., where the optical depth is small) the excited state populations can in general be much lower than their LTE values.

It is convenient at this time to define two parameters which provide insights into the physics of line transport. A measure of the relative populations of two states is given by the LTE departure coefficient:

$$b_1 \equiv \left(\frac{n_u}{n_\ell} \right) / \left(\frac{n_u}{n_\ell} \right)_{LTE} \quad (12)$$

where n_u and n_ℓ represent the populations of the upper and lower state, respectively. Thus, when $b_1 = 1$, the upper and lower state populations are related by Boltzmann statistics. The quenching parameter, which describes the collisional thermalization of a scattered photon, is given by:

$$P_Q = \frac{C_{ul}}{C_{ul} + A_{ul}(1 - e^{-h\nu/kT})^{-1}}. \quad (13)$$

A low value for the quenching parameter means a photon will be scattered many times before it is “destroyed” by a collisional deexcitation.

Figure 3 shows the LTE departure coefficients of 3 transitions for the case of a spherical argon plasma with $T = 30$ eV, $n = 3 \times 10^{16}$ cm⁻³, and $R = 1$ m. Note that the distance scale is logarithmic and is measured with respect to the outer boundary of the plasma sphere. The curves correspond to 3 resonance lines of Ar VII, Ar VIII, and Ar IX. Table 1 lists some of the properties of these transitions. All 3 lines have line center optical depths much greater than unity. However, only for the Ar VII and Ar VIII lines do the relative populations approach their LTE values in the interior of the plasma. This is because for

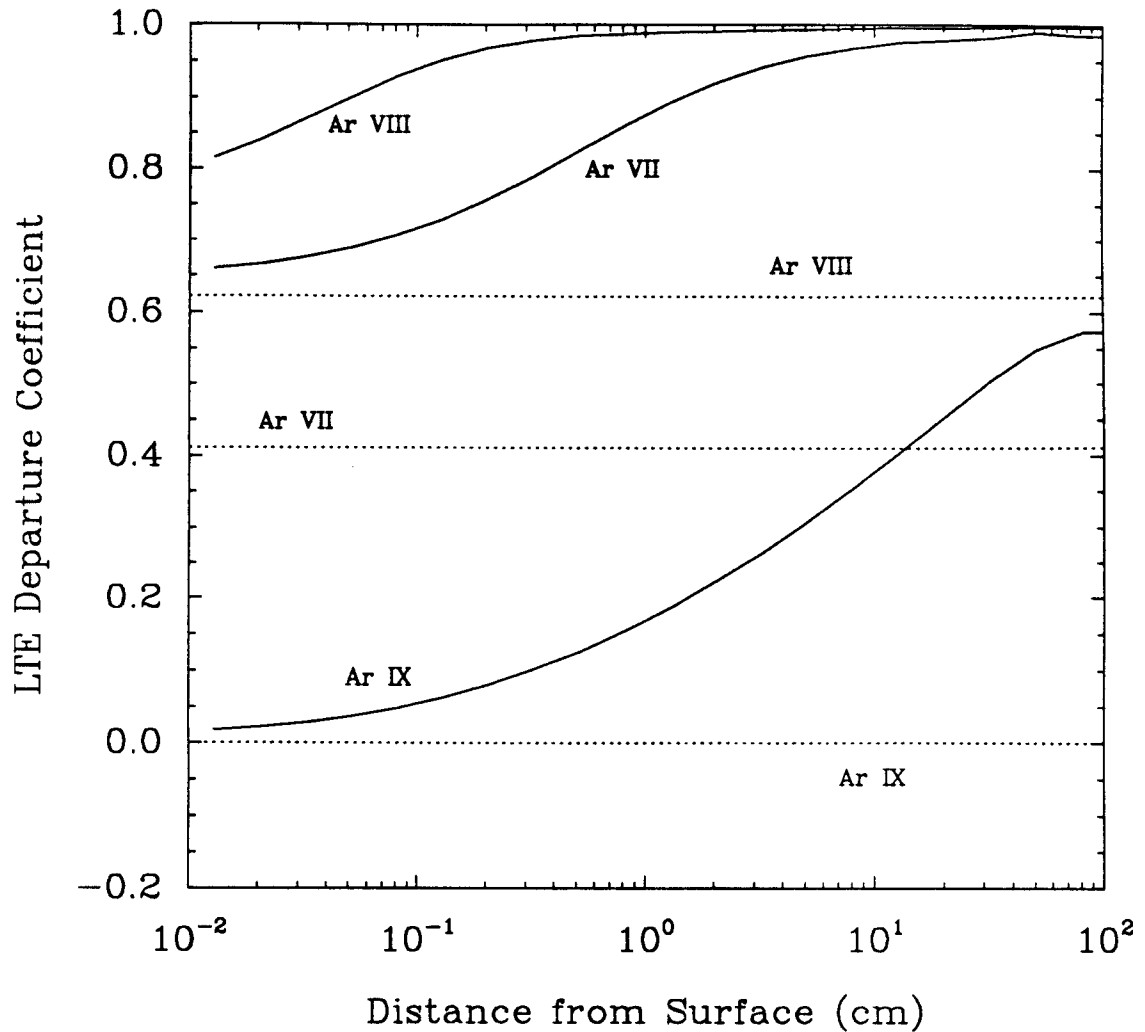


Figure 3. Dependence of LTE departure coefficients on distance from the surface of a spherical Ar plasma with $T = 30$ eV, $n = 3 \times 10^{16}$ cm $^{-3}$, and $R = 100$ cm. Solid curves represent results from non-LTE radiative transfer calculations. Results from calculations neglecting photoabsorption effects are shown as dotted lines. Results are for resonance lines of Ar VII, Ar VIII, and Ar IX whose atomic properties are listed in Table 1.

Doppler profiles the LTE departure coefficient approaches unity at optical depths greater than P_Q^{-1} .³² At optical depths less than this the excited state populations are lower because photons are able to scatter their way out of the plasma before being quenched. In effect, an atom in this region sees the absence of incident radiation at the plasma boundary.

The curves for Ar IX show an example of a transition in which the plasma is “effectively thin” to its line radiation. Even though the line center optical depths near the center of the plasma exceed 10^3 , n_u/n_l never exceeds 60% of its LTE value and falls to $\sim 10^{-2}$ at the surface. This is because the quenching parameter for the transition is so small ($P_Q = 1.8 \times 10^{-4}$) that even photons emitted in the center of the plasma can scatter their way out of the plasma before a collisional deexcitation destroys the photon.

Also shown in Fig. 3 as dashed curves are the population ratios computed in the absence of a radiation field; that is, with photoexcitation and photoionization effects neglected in the rate equations. These “thin plasma” populations are constant throughout the plasma because we have assumed the temperature and density to be uniform. For all 3 transitions it is clear that neither an LTE model ($b_1 = 1$) nor the thin plasma model accurately predict the population densities. Errors for both of these models range from roughly 20% to more than a factor of 2 for the Ar VII and Ar VIII curves. For the Ar IX line, where the thin plasma departure coefficient is 2×10^{-4} , the LTE model can overestimate the excited state population by up to 2 orders of magnitude, while the thin plasma model underestimates the population by more than 3 orders of magnitude at the center of the plasma.

The above results show that photoabsorption has a significant impact on the distribution of atomic level populations in post-explosion inertial fusion plasmas. Since plasma opacities and emissivities depend on the level populations, reliable analysis of the radiative properties of such plasmas must take this effect into consideration. The impact of neglecting photoabsorption effects on the radiation flux escaping the plasma will be discussed in Section 3.3.

3.2. Emission Spectra

We next discuss the evolution of the emission spectrum from the hot, expanding plasmas created as a result of ICF pellet explosions. Figures 4, 5, and 6 show the radiative flux at the boundary as a function of photon energy for 3 cases: $T = 1$ keV, $R = 0.3$ m (Fig. 4); $T = 30$ eV, $R = 1$ m (Fig. 5); and $T = 2$ eV, $R = 4$ m (Fig. 6). In each case the density of the argon plasma is 3×10^{16} ions/cm³. The solid lines in each figure represent the results from our non-LTE radiative transfer calculations while the dashed curves represent the blackbody curve for that temperature. It is obvious from these figures that the emission spectra from these plasmas are nothing like the blackbody spectra. The calculated spectra exhibit strong emission lines which at the lower temperatures approach the blackbody curve. Lines from He-like and Li-like Ar dominate the spectrum of the $T = 1$ keV plasma, while Ne-like, Na-like, and Mg-like Ar lines show the strongest emission lines at $T = 30$ eV. For the $T = 2$ eV plasma, lines from Ar I and Ar II have the highest fluxes. In all cases, free-free (Bremsstrahlung) emission dominates the continuum spectrum at relatively low photon energies while bound-free emission dominates at the higher photon energies.

Additional insights into the physical processes affecting these emission spectra can be obtained by examining the absorption properties of the plasma. Figures 7, 8, and 9 show the frequency-dependent optical depths for the cases shown in Figs. 4 through 6. At all 3 temperatures the plasmas are optically thick ($\tau > 1$) in at least some of the line cores. The optical depths of the most optically thick lines are roughly 10^2 , 10^4 , and 10^6 for the $T = 1$ keV, 30 eV, and 2 eV cases, respectively. The primary reason for the increase in optical depth with decreasing temperature is that the Doppler width decreases as the temperature falls: $\Delta\nu_D \sim h\nu_0 \cdot T^{-\frac{1}{2}} \sim T^{\frac{3}{2}}$.

It is also seen, particularly in the $T = 1$ keV calculation, that while some lines are optically thick their peak fluxes fall far short of the blackbody flux for that frequency. For instance, the lines near $h\nu = 3$ keV in the $T = 1$ keV calculation have optical depths which

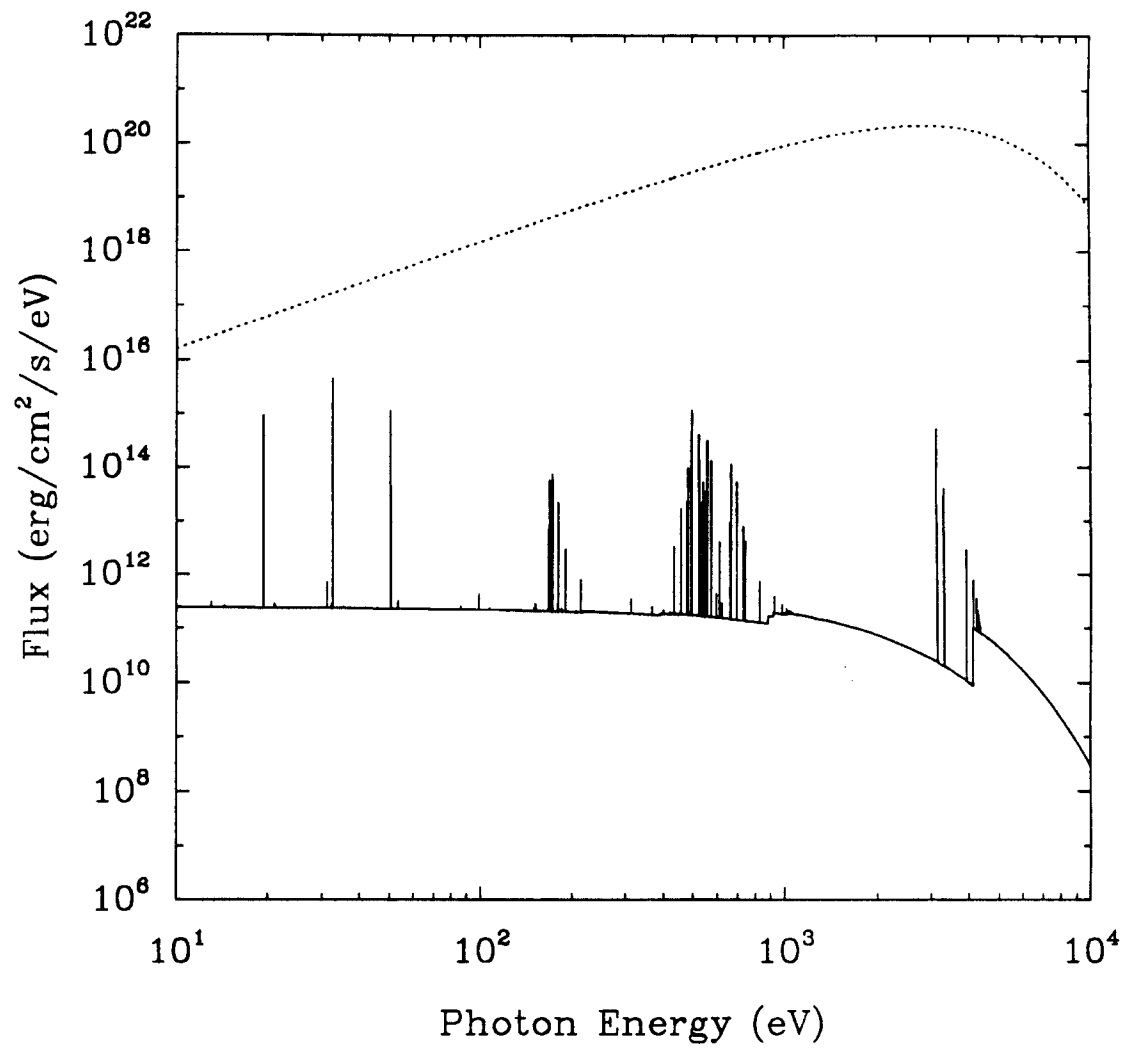


Figure 4. Spectral flux emitted at the boundary of a spherical Ar plasma at $T = 1$ keV, $n = 3 \times 10^{16}$ cm⁻³, and $R = 30$ cm. The dashed curve represents the blackbody flux.

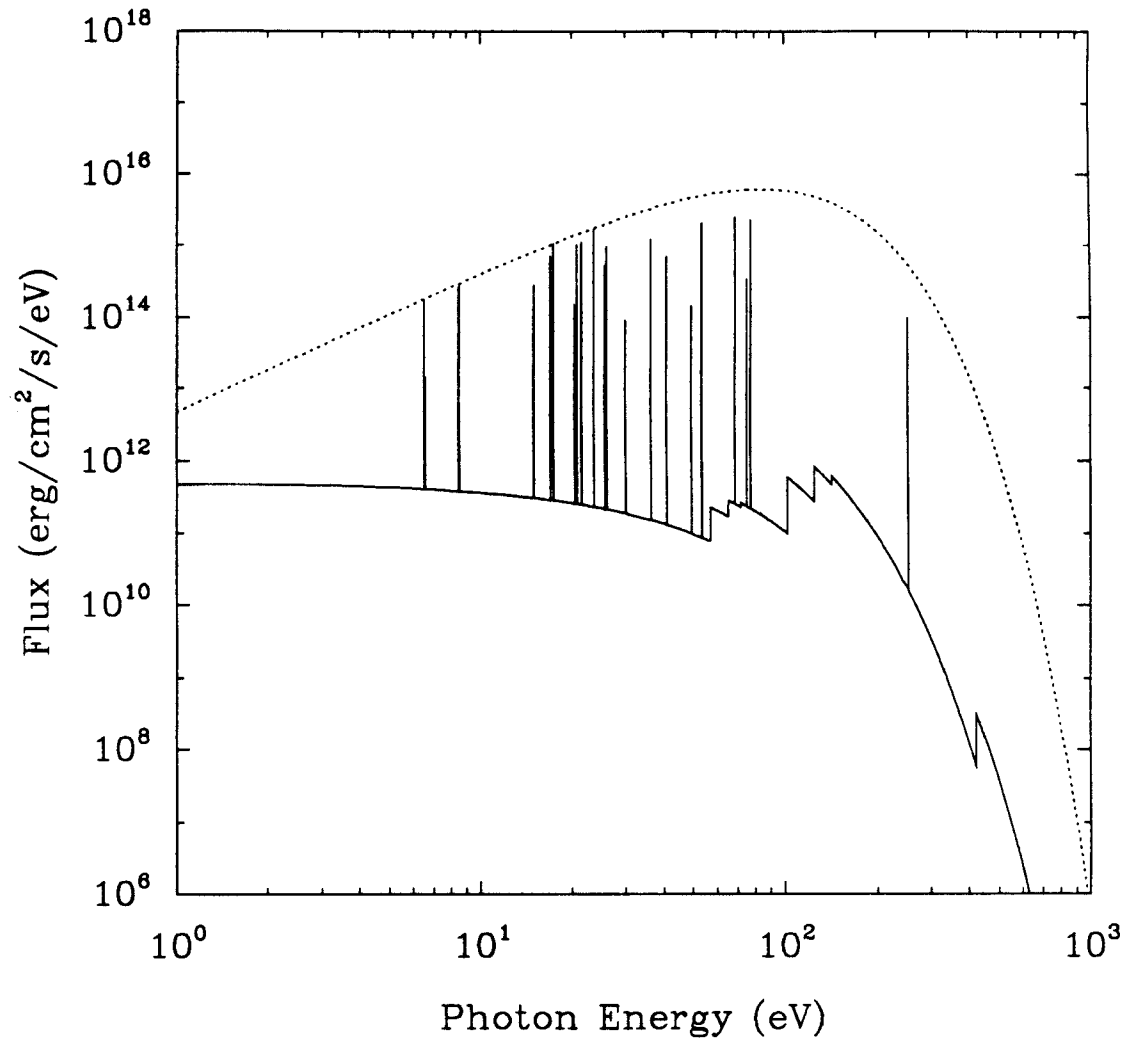


Figure 5. Spectral flux emitted at the boundary of a spherical Ar plasma at $T = 30$ eV, $n = 3 \times 10^{16}$ cm⁻³, and $R = 100$ cm. The dashed curve represents the blackbody flux.

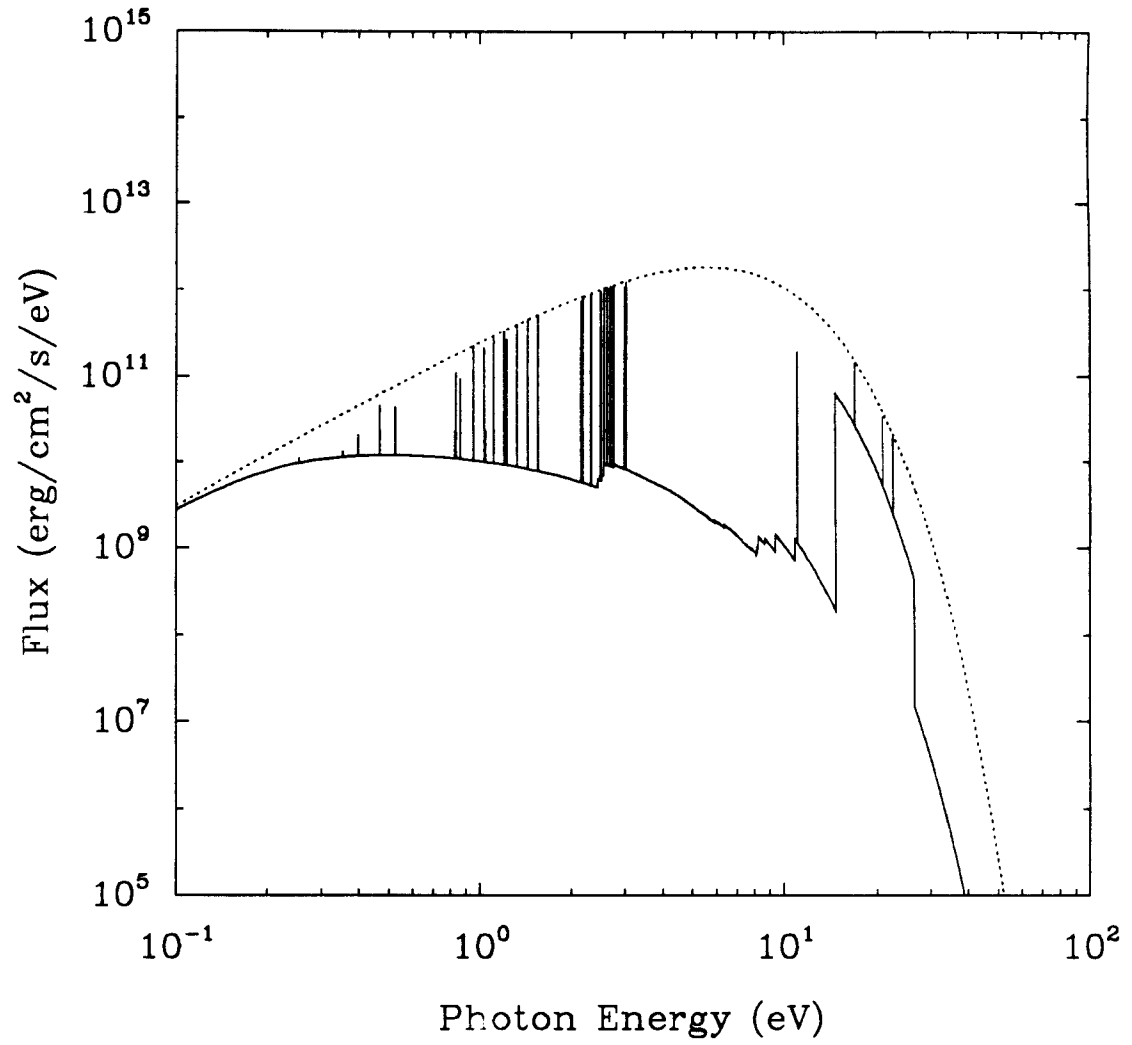


Figure 6. Spectral flux emitted at the boundary of a spherical Ar plasma at $T = 2$ eV, $n = 3 \times 10^{16}$ cm⁻³, and $R = 400$ cm. The dashed curve represents the blackbody flux.

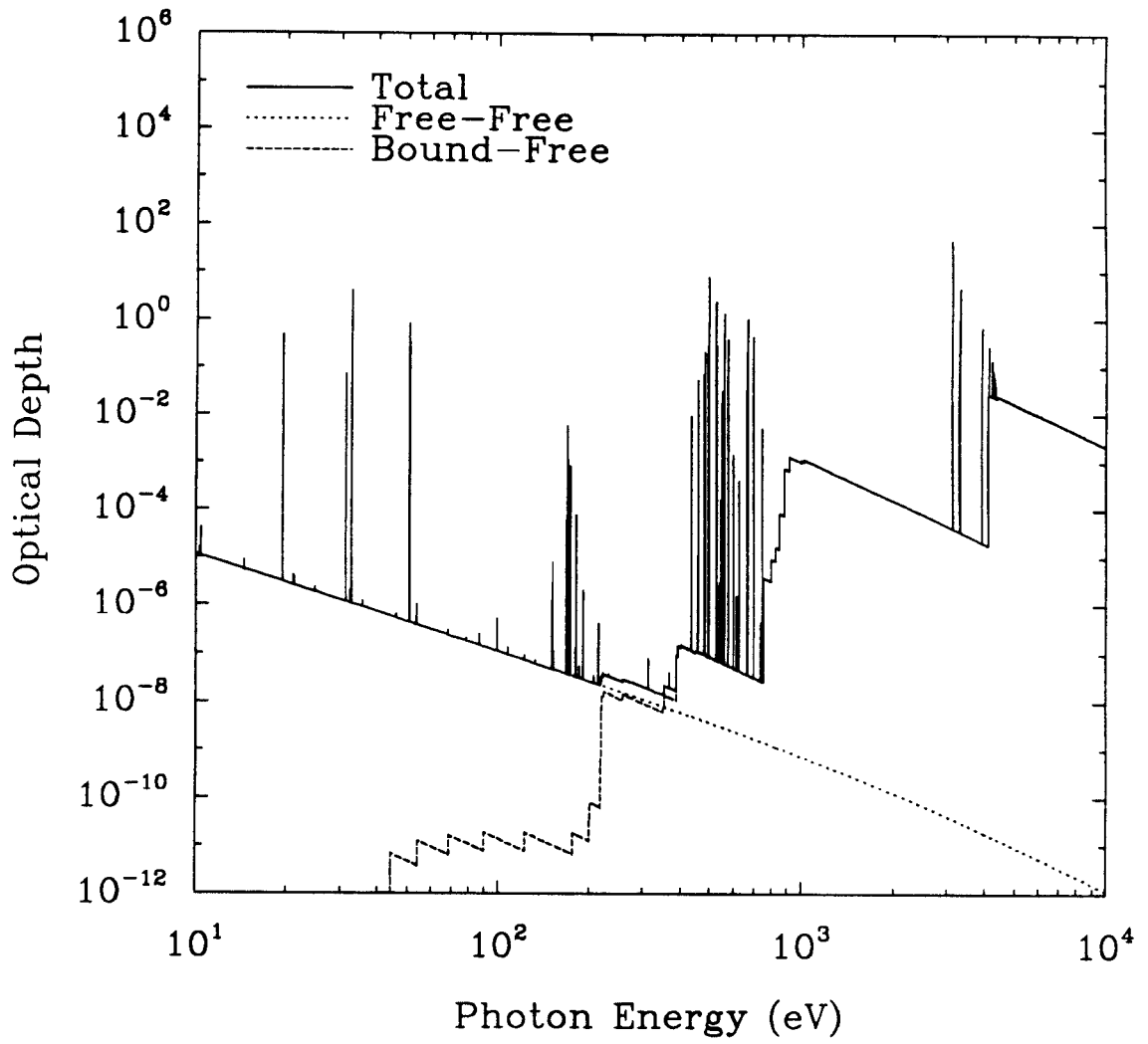


Figure 7. Frequency-dependent optical depths for the case shown in Figure 4.

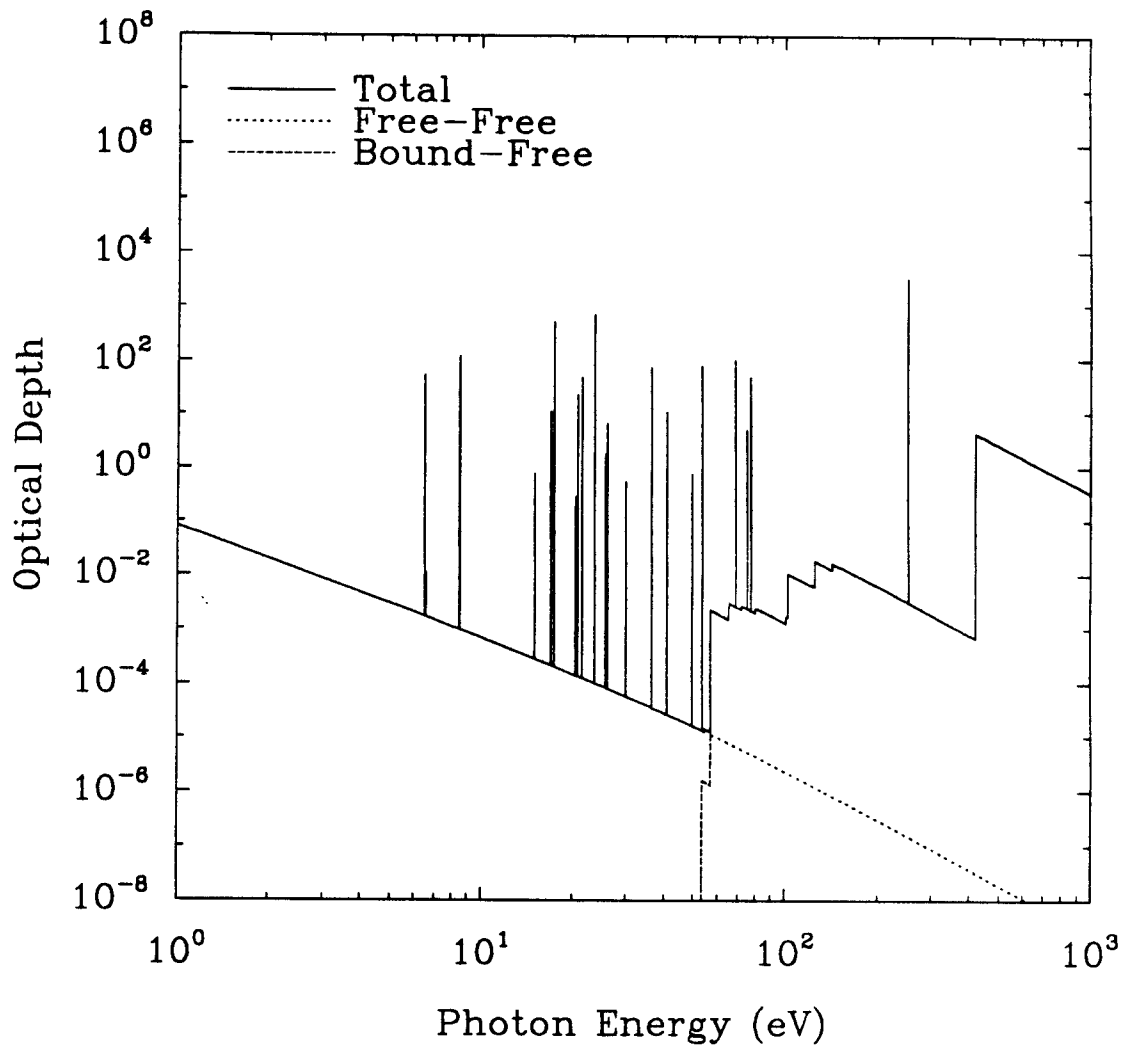


Figure 8. Frequency-dependent optical depths for the case shown in Figure 5.

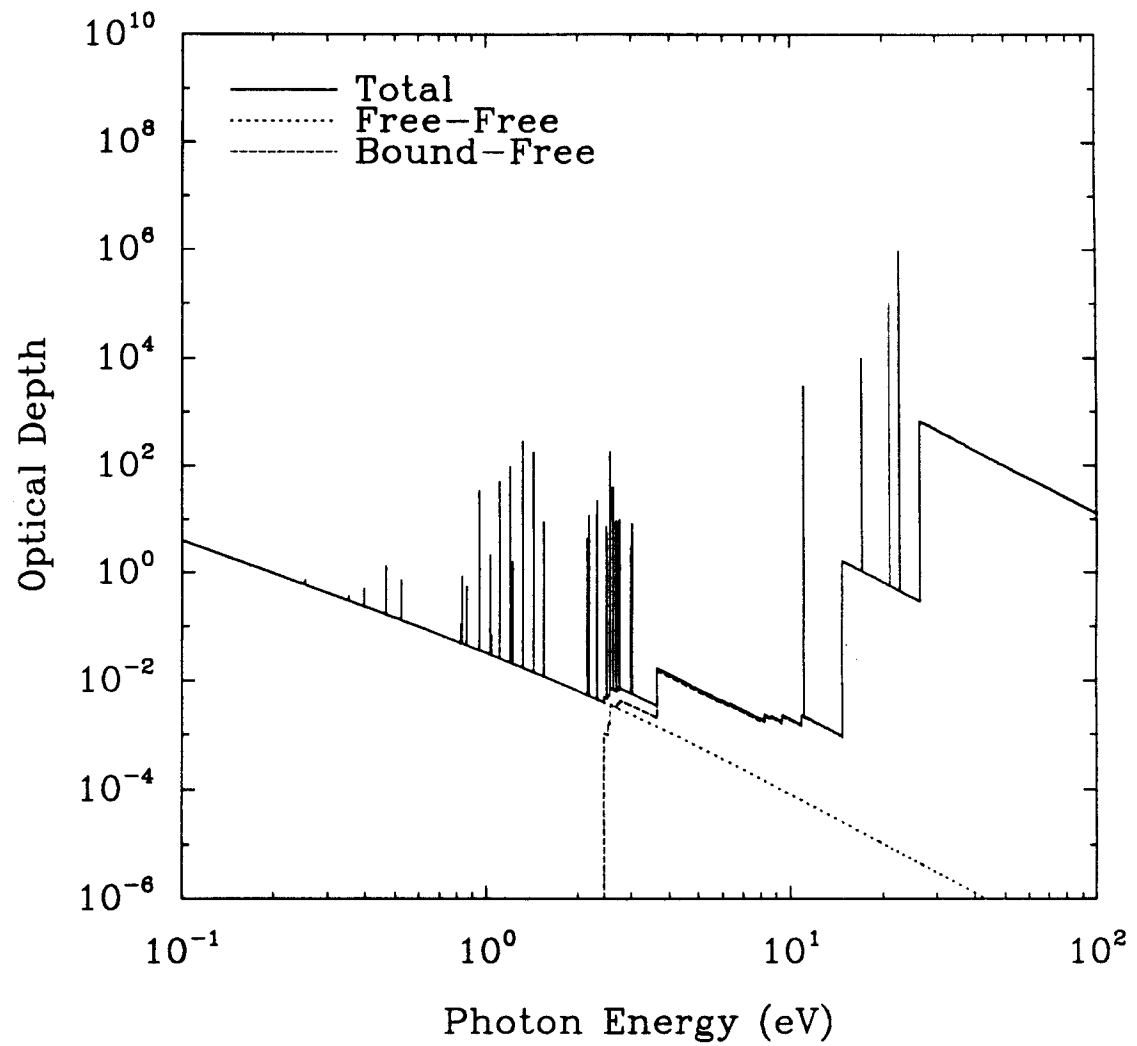


Figure 9. Frequency-dependent optical depths for the case shown in Figure 6.

exceed unity (Fig. 7), but their fluxes are 5 orders of magnitude lower than the blackbody flux (Fig. 4). This results from the fact that the quenching parameters tend to be lower for lines in higher temperature plasmas, causing the populations of the excited states to fall far below their LTE values. In the $T = 2$ eV calculation, the line center optical depths are higher and the quenching parameters of many lines are near unity. This results in lines which rise up to the blackbody curve.

The reason for the appearance of strong emission lines in plasmas of this type is that the continuum is optically thin at most wavelengths. Only at the lower temperatures and relatively high photon energies do the plasmas become optically thick to bound-free absorption. Even in these cases, the continuum flux in this spectral region is significantly below the blackbody flux (see Fig. 6 at $h\nu > 12$ eV) because the LTE departure coefficients for bound-free transitions are much below unity for plasmas at this density.³³ The plasmas are almost always optically thin to free-free transitions except at the lowest temperatures and at rather low photon energies ($h\nu < 0.2$ eV in Fig. 9).

It is also instructive to examine the dependence of the radiation spectral flux on the gas density. This is shown in Fig. 10, where the results of three calculations are shown and compared to the blackbody curve. In each case the plasma temperature is 30 eV and the radius is 1 m. The densities are 3×10^{16} cm⁻³ (lower curves), 3×10^{18} cm⁻³ (middle curves) and 3×10^{20} cm⁻³ (top curves). The corresponding results for the frequency-dependent optical depths are shown in Fig. 11.

Note that as the plasma density increases the spectral flux increases to the point where it essentially is equivalent to the blackbody spectrum at $n = 3 \times 10^{20}$ cm⁻³. The reason for the observed dependence can be understood by examining Fig. 11. For the $n = 3 \times 10^{16}$ cm⁻³ calculation, the continuum optical depths are less than unity for all photon energies except those between 400 and 700 eV. As a result, the continuum flux lies far below the blackbody curve. At $n = 3 \times 10^{18}$ cm⁻³, the plasma is optically thick to free-free emission at photon

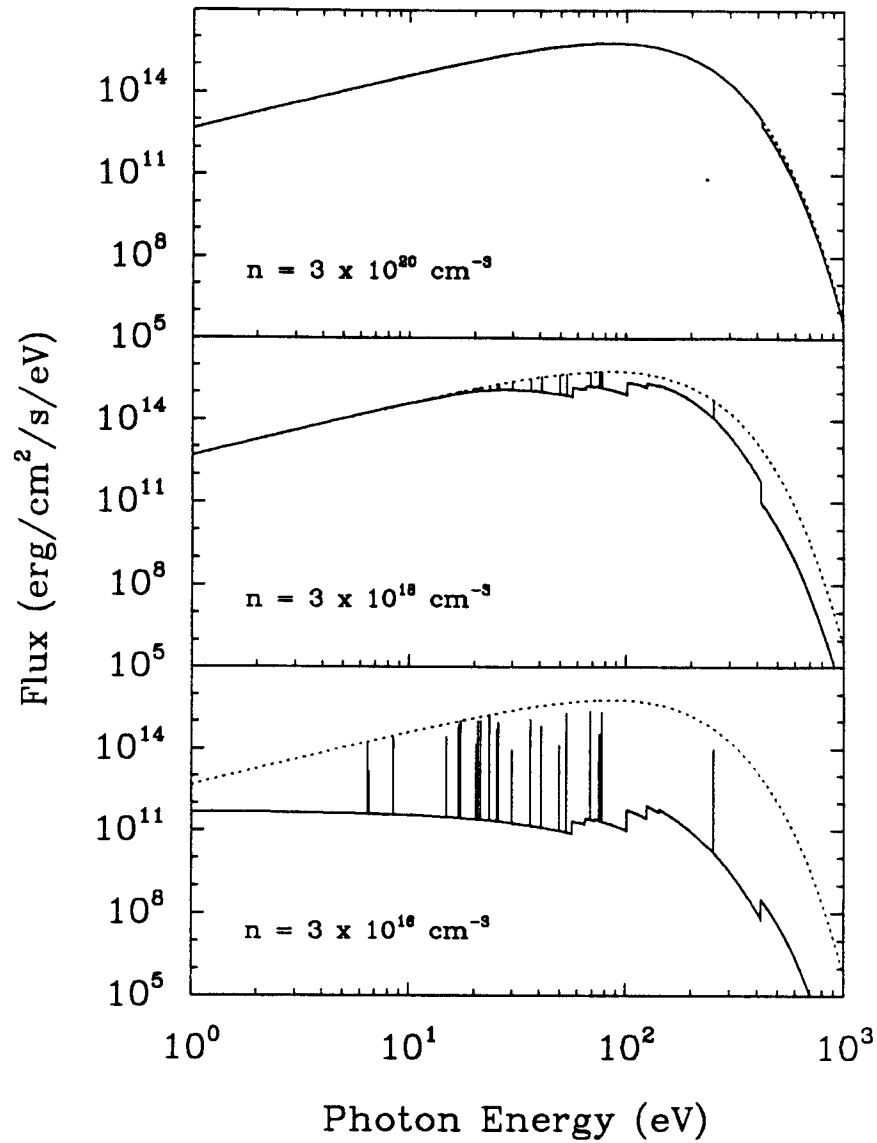


Figure 10. Dependence of the spectral flux emitted at the boundary of a spherical Ar plasma on density. In each case $T = 30 \text{ eV}$ and $R = 100 \text{ cm}$. The dashed curve represents the blackbody flux.

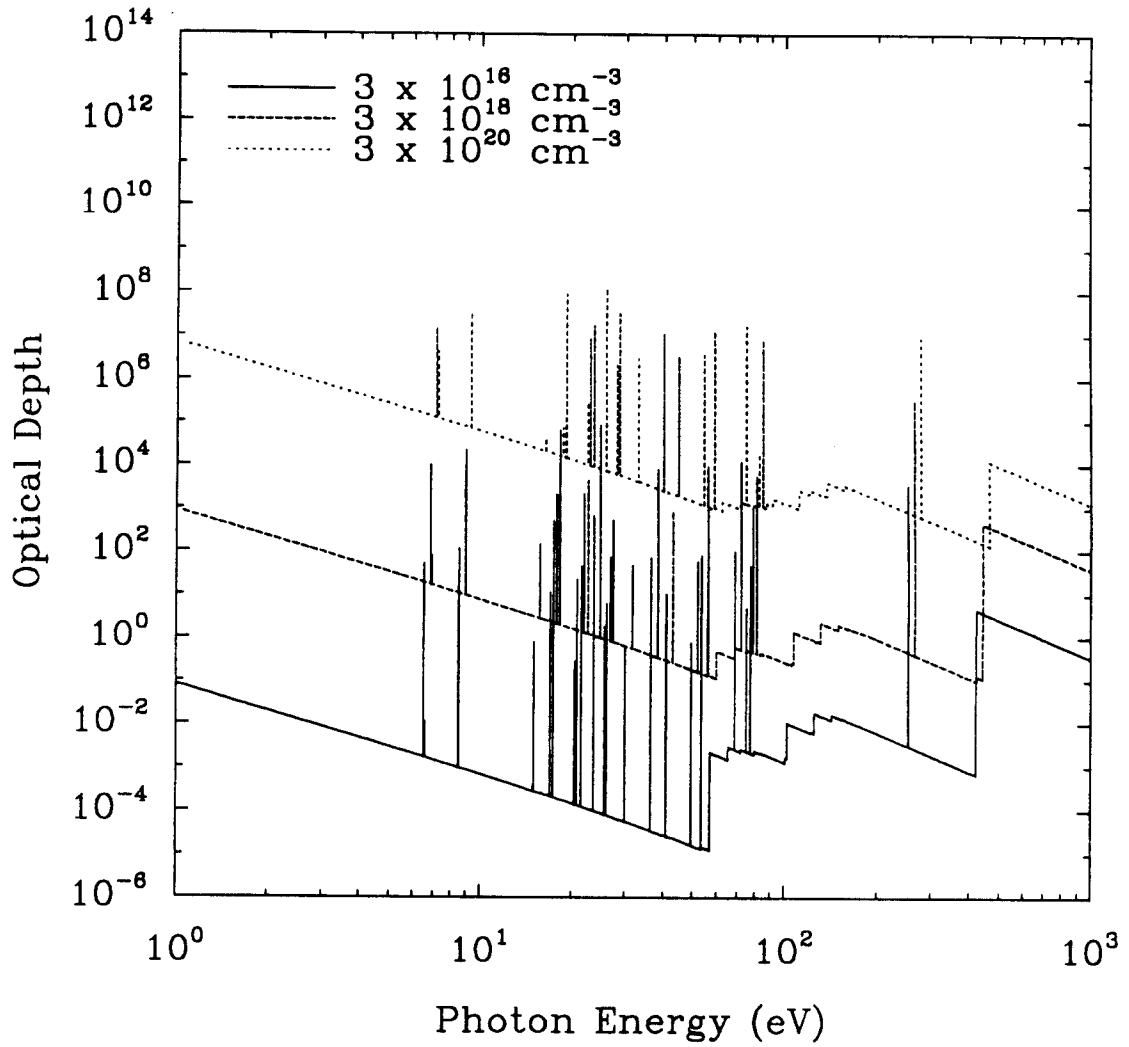


Figure 11. Dependence of optical depths on density for spherical Ar plasmas with $T = 30$ eV and $R = 100$ cm. The curves for the 2 higher density cases have been offset slightly in the horizontal direction for clarity.

energies below 20 eV. Because of this, the spectral flux lies close to the blackbody curve at these low frequencies, and lies somewhat below it at higher frequencies. At the highest density, the computed flux is virtually identical to the blackbody curve, with the exception of a small absorption edge near 400 eV. This again is caused by the ionization populations being slightly out of LTE.

The above results show very clearly that the radiation field in plasmas created by high-gain inertial fusion explosions is neither blackbody nor does it vary smoothly with photon energy. The latter point presents a major difficulty for radiation transport models which divide the frequency spectrum into a modest ($\sim 10^1 - 10^2$) number of energy groups. In addition, we have seen how the self-absorption of line radiation prevents the flux at the centers of optically thick lines from exceeding the blackbody flux. Because of the detailed atomic model used in these calculations, it would also be possible to attempt to deduce plasma conditions from line spectra obtained in such plasmas. This analysis will be performed in future investigations.

3.3. Radiative Energy Losses and Comparison with Other Models

We next examine the rate at which radiative energy escapes the plasma. We shall also compare our results to those from a variety of other models that are commonly used to study the radiative properties of high-temperature plasmas. Tables 2 through 4 list the calculated radiation power densities (i.e., the energy escaping the plasma per second per unit volume) for several models. The first model is our non-LTE radiative transfer model, which is a collisional-radiative equilibrium model that includes the effects of photoexcitation and photoionization on the atomic level populations. We consider the results from this model to be the most reliable. The second row shows the power densities calculated when LTE level populations are assumed. The third row shows results for a CRE model which neglected the effects of photoabsorption on the level populations. In the optically thin model, the populations were calculated in the same way as the CRE model without photoabsorption,

but in this case the calculated power density neglects all attenuation effects. The last row lists results calculated for a blackbody (thermal equilibrium) model.

In the top four models in Tables 2 through 4, the power densities were computed using the same computer code but with various physical processes neglected. At each temperature, we used an identical atomic level structure with the same number of levels, the same spatial grid, and same atomic data. Thus, the differences that arise in the first 3 models are due solely to the differences in the level populations, while in the thin plasma model additional differences arise because attenuation effects are neglected.

For all models except the blackbody case, the power density contributions from Bremsstrahlung (free-free), photorecombinations (bound-free), and lines (bound-bound) are listed. Note that the non-LTE radiative transfer calculations (top row) show the power densities are dominated by line emission at high temperatures and continuum emission at low temperatures. The decline of the relative importance of line emission occurs for 3 reasons. First, at temperatures \lesssim a few eV, both the velocities and the number of the free electrons decreases. This leads to small collisional excitation rates which in turn reduces the number of excited state atoms capable of emitting photons. Second, the ability of the plasma to quench a scattering photon increases as the temperature decreases. And third, the line center optical depth increases at lower temperatures due to decreased Doppler broadening. As a result, line radiation emitted from the interior of the plasma is absorbed and quenched before it escapes. The only line radiation that escapes is that which is emitted very close to the “edge” of the plasma.

The LTE power densities exceed the non-LTE transport values by a factor of between 2 and 5. At all temperatures, the continuum power densities (both bound-free and free-free) are substantially higher in the LTE case. This occurs because the mean ionization of the LTE plasma is higher. The magnitude of the discrepancy shows the importance of radiative

recombination in plasmas at these conditions. The higher LTE line power densities also indicate the excited states are overpopulated, particularly near the plasma surface.

The effects of including photoabsorption when computing the atomic populations can be seen by comparing the results in the first and third rows of Tables 2, 3, and 4. At each temperature the power densities are lower when photoabsorption effects are neglected. This is particularly true for line radiation at temperatures above a few eV, where the line power densities are a factor of about 5 to 7 too low in the calculation neglecting photoabsorption. This results from the fact that the excited state populations in the interior of the plasma are significantly enhanced through the photoexcitation process.

The power densities calculated using the optically thin model are in each case higher than those in the non-LTE radiative transfer calculation. For the $T = 2$ eV and $T = 30$ eV calculations, the line power densities are 2 to 3 orders of magnitude too high in the optically thin case. Although the excited state populations are underestimated in this model, the rate at which radiative energy escapes the plasma is seriously overestimated because each photon emitted in the plasma is assumed to escape.

Note, however, that at very high temperatures the plasma becomes “effectively thin”. This is evident from the fact that the non-LTE transport power density and optically thin power density are within a few percent of each other. The continuum powers are virtually identical because the plasma is optically thin to continuum radiation (see Fig. 7). The plasma is effectively thin to line radiation because the ability of the plasma to quench scattered photons is weak ($P_Q \ll \tau_{\text{line}}^{-1}$).

Also shown in Tables 2 through 4 are the power densities calculated assuming a blackbody radiation model. In each case the blackbody model grossly overestimates the radiation flux escaping the plasma: by 2 orders of magnitude at $T = 2$ eV and by more than 8 orders of magnitude at $T = 1$ keV. The reason is that there is simply not enough mass present for the plasma to be optically thick at all frequencies.

We have also compared our results to those from a multigroup radiation diffusion model. The radiation diffusion model utilized is part of a radiation-hydrodynamics code that is used to study time-dependent phenomena in ICF target chamber plasmas.³⁴ Multigroup opacities were computed with a hydrogenic ion code³⁵ which considers the same physical processes as our non-LTE radiative transfer model with the exceptions of photoexcitation and photoionization. Thus, the model is similar to the “CRE without photoabsorption” model in Tables 2 through 4, but with the following differences: (1) radiation is transported in a modest number of photon energy groups whose widths are very large compared to the widths of line radiation; and (2) the atomic data (rate coefficients, energy levels, etc.) are less accurate.

A series of calculations was performed in which the number of photon energy groups was varied between 20 and 160. Figure 12 shows the calculated power density as a function of the number of energy groups. It is clear that the computed power depends sensitively on the number of groups, and that even at 160 groups the radiated power continues to decrease as the number of groups increases.

The reason for the observed dependence on the number of groups can be understood as follows. Multigroup radiation diffusion models generally use opacities which represent an average of the plasma absorption or emission over some predefined range in photon energy. Planck mean opacities are often employed to compute the rate at which energy is exchanged between the plasma and the radiation field, while Rosseland mean opacities are used to transport radiation.^{21,36} The Planck and Rosseland mean opacities are, respectively, defined by

$$\bar{\kappa}_{\text{P}} = \frac{\int \kappa_{\nu} B_{\nu} d\nu}{\int B_{\nu} d\nu}$$

and

$$\bar{\chi}_{\text{R}} = \frac{\int \frac{\partial B_{\nu}}{\partial T} d\nu}{\int \frac{1}{\chi_{\nu}} \frac{\partial B_{\nu}}{\partial T} d\nu}, \tag{14}$$

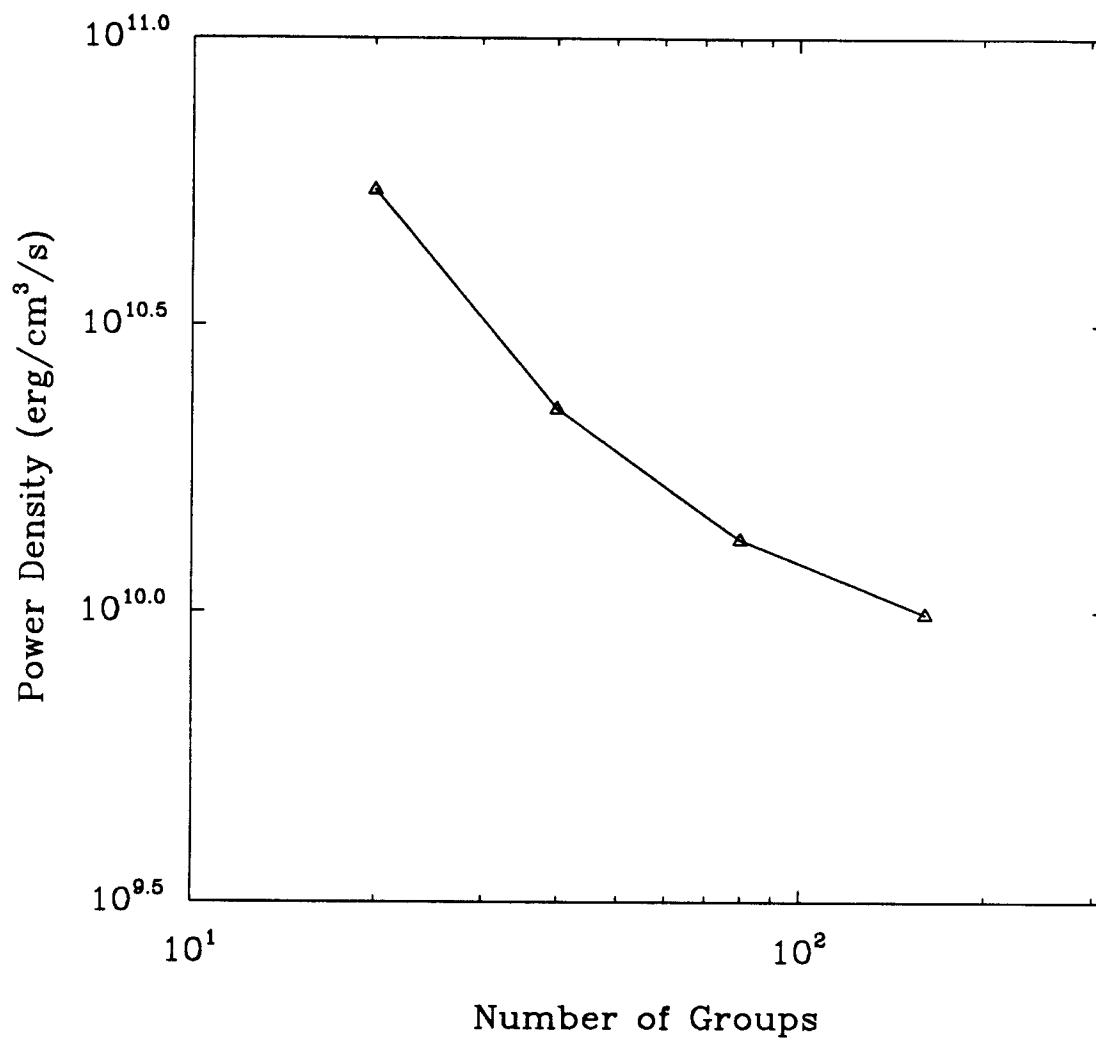


Figure 12. Dependence of the total power density calculated using a multigroup radiation diffusion model on the number of photon energy groups.

where B_ν is the Planck function, κ_ν is the absorption coefficient, and χ_ν is the extinction coefficient (equal to the sum of the absorption coefficient and the scattering coefficient). The key point is that the Rosseland mean, by using the *reciprocal* of the extinction coefficient, gives the greatest weight to where the absorption is lowest; that is, the continuum. Line cores, which can have absorption coefficients orders of magnitude higher than the continuum, contribute little to the Rosseland mean. However, the Planck mean puts greatest weight where the absorption is highest; i.e., the lines. Thus in the multigroup radiation diffusion model, the rate at which energy is exchanged between the plasma and the radiation field is strongly influenced by lines, while the radiation is being transported at a rate that is essentially determined using continuum opacities. But because the plasmas of interest are often optically thin at continuum frequencies, the energy being transferred from the plasma to the radiation field quickly escapes rather than being re-thermalized by the plasma.

This effect can also be seen in Fig. 13, where the spectral flux computed using the multigroup radiation diffusion model with 20 groups (dashed curve) is compared with that from the non-LTE radiative transport model (solid curve). In both calculations the temperature was 2 eV, the density was $3 \times 10^{16} \text{ cm}^{-3}$, and the radius of the spherical argon plasma was 4 meters. Also shown (dotted curve) is the blackbody spectrum for a $T = 2 \text{ eV}$ plasma. Like the non-LTE radiative transfer model, line emission causes the flux in the multigroup diffusion calculation to rise up to near the blackbody curve. However, because the widths of the energy groups are much larger than the actual line widths, the magnitude of the escaping flux is much higher in the multigroup calculation (by a factor of 34 in the 20-group case). This overestimation of the flux is rooted in the way in which multigroup opacities are obtained.

It is important to note that an accurate prediction of the flux cannot be obtained with a multigroup radiation diffusion model by simply using a very large number of photon energy groups, as has been done to study laser-generated plasma expansions³⁷ as well as ICF

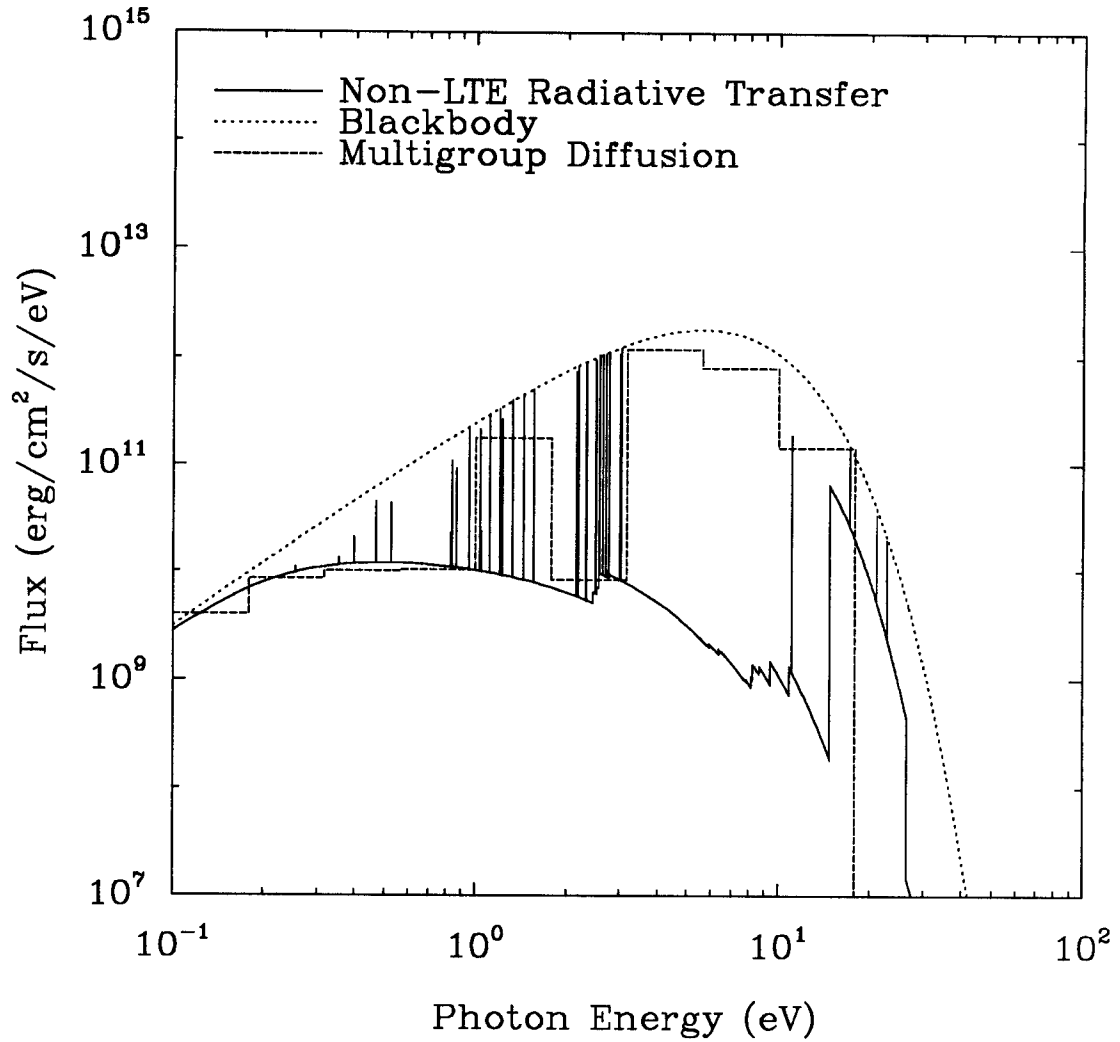


Figure 13. Comparison of frequency-dependent flux at the surface of a spherical Ar plasma calculated using a non-LTE radiative transfer model, a multigroup radiation diffusion model, and a blackbody model. The plasma conditions are $T = 2$ eV, $n = 3 \times 10^{16}$ cm $^{-3}$, and $R = 400$ cm.

target chamber plasmas.¹³ This is because the atomic level populations depend sensitively on the characteristics of the radiation field. Thus, the opacities depend not only on the local temperature and density, but also on the radiation field. If an extremely large number of groups were to be used, the flux computed using the multigroup diffusion model would actually *underestimate* the flux because the emissivities and opacities it uses are computed using a model similar to the “CRE model without photoabsorption” model described above. As Tables 2 through 4 indicate, this model typically underestimates the flux by a factor of a few.

4. Conclusions

The results discussed in this paper demonstrate the fundamental role of photoabsorption effects in plasmas created shortly after the release of energy from high-gain inertial fusion targets. We have shown that these plasmas are often optically thick in the cores of lines while being optically thin at continuum frequencies. Because of this, line self-attenuation plays an important role both in altering the atomic level populations and in reducing the rate at which radiation escapes the plasma.

The results of our non-LTE radiation transport calculations were compared with those from a variety of other models commonly used to study high-temperature plasmas. We have shown that neglecting the effects of photoexcitation on the level populations leads to underestimates of the radiation flux by a factor of a few. On the other hand, assuming the populations are in LTE leads to overestimates by a factor of a few. Worse yet, thermal equilibrium (blackbody) models typically predict fluxes that are several orders of magnitude too large.

We have also shown that multigroup radiation diffusion models suffer from two aspects. First, it is difficult to group together optically thick lines and the optically thin continuum in a way which reliably models the exchange and transport of energy. The source of this problem stems from the fact that because the continuum is optically thin, radiation emitted by

the plasma quickly escapes before being absorbed and re-thermalized. The second problem arises from the fact that multigroup diffusion models generally use tabulated opacities that neglect the effects of photoexcitation on the atomic level populations. While the grouping approximation leads to predictions in the fluxes that are too high, neglecting photoexcitation effects will lead to fluxes which are too low. Unfortunately, the errors introduced by these 2 approximations do not cancel, and we have found that multigroup diffusion models can lead to errors in the flux that range from a factor of a few to more than an order of magnitude.

It is also worth pointing out that the line trapping effects described in this paper are also important in other types of laboratory and fusion-related plasmas. Laser-generated plasma expansions have been used to observe the formation and evolution of blast waves in moderate-density gases.^{38,39} Numerical simulations of these experiments⁴⁰ found that better agreement with the experimental data was obtained when radiative energy losses were ignored than when a radiative diffusion model was employed. It now appears the diffusion model grossly overestimated the rate at which energy escaped the plasmas, which resulted in weaker, lower velocity shocks. Also, discharge Z-pinches have been proposed^{41,13} for ICF facilities as a way to confine light ions as they are transported from the diode to the target. These plasmas, which are also optically thick to line radiation and optically thin to continuum radiation, will be subject to many of the same effects discussed above.

The importance of these effects for energy transport in moderate-density inertial fusion plasmas and the ramifications for the design of and potential damage to target chambers for high-gain facilities are significant. A lower radiation flux at exposed solid surfaces can produce lower thermal and mechanical stresses and a slower rate of erosion. This is because the temperature rise in the absorbing surface layer depends on the competition between the radiation flux onto the layer and energy transport by thermal conduction through the solid material. These comments are also relevant to any other material that is exposed to

the plasma radiation flux, such as the final optics in a laser-driven fusion facility⁴² or the diodes or magnets in an ion-driven fusion facility.¹³ In addition, the strength of the shock in the expanding plasma will be affected by the rate at which radiative energy escapes the plasma.

Radiative transfer and hydrodynamics will play a critical role in energy transport within high-gain ICF target chambers. Additional work needs to be done to gain a firmer understanding of these processes. Unanswered questions include: what effect do fluid velocity gradients have on the escaping radiation flux? what role does continuum-induced photoexcitation play in altering the atomic level populations and the flux? and how is the shock strength modified by line self-attenuation effects? We intend to study these and other questions in future theoretical investigations. In addition, experimental studies could lead to a significantly better understanding of these effects. Such experiments will likely be required before high-gain ICF facilities are constructed.

Acknowledgements

This work has been supported in part by the U.S. Department of Energy through Sandia National Laboratories. Computing support has been provided in part by the U.S. National Science Foundation through the San Diego Supercomputing Center.

References

1. Clark, R.W., Davis, J., and Cochran, F.L., *Phys. Fluids* **29**, 1971 (1986).
2. Spielman, R., and Palmer, M.A., *Bull. Am. Phys. Soc.* **24**, 1361 (1984).
3. Dietrich, K.-G., Mahrt-Olt, K., Jacoby, J., Boggasch, E., Winkler, M., Heimrath, B., and Hoffmann, D.H.H., *Lasers and Particle Beams* **8**, 583 (1990).
4. Kunze, H., Noll, R., Haas, C.R., Elfers, M., Hertzberg, J., and Herziger, G., *Lasers and Particle Beams* **8**, 595 (1990).
5. Duston, D., Clark, R.W., Davis, J., and Apruzese, J.P., *Phys. Rev. A* **27**, 1441 (1983).
6. Duston, D., Clark, R.W., and Davis, J., *Phys. Rev. A* **31**, 3220 (1985).
7. Rogerson, J.E., Clark, R.W., and Davis, J., *Phys. Rev. A* **31**, 3323 (1985).
8. MacFarlane, J.J., Wang, P., and Moses, G.A., *Lasers and Particle Beams*, in press (1991).
9. Badger, B., *et al.*, Report No. UWFDM-450, Fusion Technology Institute, University of Wisconsin, Madison, WI, 1981 (unpublished).
10. Pitts, J.H., *Fusion Tech.* **8**, 1198 (1985).
11. Blink, J.A., Hogan, W.J., Hovingh, J., Meier, W., and Pitts, J.H., Report No. UCRL-53559, Lawrence Livermore National Laboratory, Livermore, CA, 1985 (unpublished).
12. Sviatoslavsky, I.N., Sawan, M.E., Moses, G.A., Kulcinski, G.L., Engelstad, R.L., Larsen, E., Lovell, E., MacFarlane, J.J., Peterson, R.R., and Wittenberg, L.J., *Proceedings of the IEEE 13th Symposium on Fusion Engineering, Knoxville, TN*, edited by M. Lubell, M. Nestor, and S. Vaughan (IEEE, New York, 1990), p. 1416.

13. Moses, G.A., *et al.*, in *Beams '88, Proceedings of the Seventh International Conference on High-Power Particle Beams*, edited by W. Bauer and W. Schmidt (Karlsruhe, 1988).
14. *LMF - Laboratory Microfusion Capability Study: Phase I Summary*, U.S. Dept. of Energy, Inertial Fusion Division, Washington, DC (1989).
15. MacFarlane, J.J., Peterson, R.R., and Moses, G.A., *Fusion Technology* **15**, 557 (1989).
16. Engelstad, R.L., Powers, J.W., and Lovell, E.G., *Fusion Technology* **19**, 697 (1991).
17. Powers, J.W., Lovell, E.G., Sviatoslavsky, I.N., and Engelstad, R.L., *Fusion Technology* **19**, 740 (1991).
18. MacFarlane, J.J., Moses, G.A., and Peterson, R.R., *Nucl. Fusion* **29**, 27 (1989).
19. Glenn, L.A., *Nucl. Engr. and Design* **64**, 357 (1981).
20. MacFarlane, J.J., Moses, G.A., Peterson, R.R., and Sviatoslavsky, I.N., *Proceedings of the IEEE 13th Symposium on Fusion Engineering, Knoxville, TN*, edited by M. Lubell, M. Nestor, and S. Vaughan (IEEE, New York, 1990), p. 746.
21. Mihalas, D., *Stellar Atmospheres, Second Edition* (Freeman, New York, 1978).
22. MacFarlane, J.J., Wang, P., and Moses, G.A., Report No. UWFDM-822, Fusion Technology Institute, University of Wisconsin, Madison, WI, 1990 (unpublished).
23. MacFarlane, J.J., Wang P., and Moses, G.A., *Lasers and Particle Beams* **8**, 729 (1990).
24. MacFarlane, J.J., Wang, P., and Henderson, D.L., Report No. UWFDM-847, Fusion Technology Institute, University of Wisconsin, Madison, WI, 1991 (unpublished).
25. Wang, P., *Computation and Application of Atomic Data for ICF Plasmas*, Ph.D. Dissertation, Dept. of Nuclear Engineering and Engineering Physics, University of Wisconsin, Madison, WI (1991).

26. Apruzese, J.P., Davis, J., Duston, D., and Whitney, K.G., *J.Q.S.R.T.* **23**, 479 (1980).
27. Apruzese, J.P., *J.Q.S.R.T.* **25**, 419 (1981).
28. Sobelman, I.I., Vainshtein, L.A., and Yukov, E.A., *Excitation of Atoms and Broadening of Spectral Lines* (Springer-Verlag, New York, 1981).
29. Burgess, A., and Summer, H.P., *Mon. Not. R. Astr. Soc.* **174**, 345 (1976).
30. Post, D.D., Jensen, R.V., Tortar, C.V., Grasberger, W.H., and Lokke, W.A., *At. Data Nucl. Data Tables* **20**, 397 (1977).
31. McQuarrie, D.A., *Statistical Mechanics* (Harper and Row, New York, 1976).
32. Avrett, E.H., and Hummer, D.G., *Mon. Not. R. Astr. Soc.* **130**, 295 (1965).
33. Dietz, R.D., and House, L.L., *Astrophys. J.* **141**, 1393 (1965).
34. Peterson, R.R., MacFarlane, J.J., and Moses, G.A., Report No. UWFDM-670, Fusion Technology Institute, University of Wisconsin, Madison, WI, 1988 (unpublished).
35. MacFarlane, J.J., *Comput. Phys. Commun.* **56**, 259 (1989).
36. Moses, G.A., Peterson, R.R., and McCarville, T.J., *Comput. Phys. Commun.* **36**, 249 (1985).
37. Giuliani, J.L., and Mulbrandon, M., *Phys. Fluids* **B1**, 1463 (1989).
38. Ripin, B.H., Ali, A.W., Griem, H.R., Grun, J., Kacenjar, S.T., Manka, C.K., McLean, E.A., Mostovych, A.N., Obenschain, S.P., and Stamper, J.A., in *Laser Interaction and Related Plasma Phenomena*, edited by G. Miley and H. Hora (Plenum, New York, 1986), Vol. 7, p. 857.

39. Kacenjar, S., Hausman, M., Keskinen, M., Ali, A.W., Grun, J., Manka, C.K., McLean, E.A., and Ripin, B.H., *Phys. Fluids* **29**, 2077 (1986).
40. MacFarlane, J.J., Moses, G.A., and Peterson, R.R., *Phys. Fluids* **B 1**, 635 (1989).
41. Freeman, J.R., Baker, L., and Cook, D.L., *Nucl. Fusion* **22**, 383 (1982).
42. MacFarlane, J.J., Peterson, R.R., Corradini, M.L., Moses, G.A., Bang, K.H., and Barry, J.J., Report No. UWFDM-793, Fusion Technology Institute, University of Wisconsin, Madison, WI, 1989 (unpublished).

Table 1.
Atomic Properties of Transitions in Figure 3.

Ion	Upper Level	Lower Level	Transition Energy (eV)	Line Center Optical Depth*	Quenching Parameter
Ar VII	$1s^2 2s^2 2p^6 3s^1 3p^1 \ ^1P$	$1s^2 2s^2 2p^6 3s^2 \ ^1S$	21.4	47	0.27
Ar VIII	$1s^2 2s^2 2p^6 3p^1 \ ^2P$	$1s^2 2s^2 2p^6 3s^1 \ ^2S$	17.4	517	0.42
Ar IX	$1s^2 2s^2 2p^5 3s^1 \ ^1P$	$1s^2 2s^2 2p^6 \ ^1S$	253	3,320	1.8×10^{-4}

*Measured along a ray from the center of the sphere to the boundary.

Table 2.
Calculated Power Densities for an Argon Plasma with
 $T = 1 \text{ keV}$, $n = 3 \times 10^{16} \text{ cm}^{-3}$, and $R = 30 \text{ cm}^*$.

Model	Free-Free	Bound-Free	Bound-Bound	Total
CRE with Photoabsorption	2.44 (13)	2.28 (13)	2.54 (14)	3.01 (14)
LTE	3.38 (13)	2.15 (14)	7.17 (14)	9.66 (14)
CRE without Photoabsorption	2.44 (13)	2.27 (13)	4.69 (13)	7.20 (13)
Optically Thin	2.45 (13)	2.29 (13)	2.63 (14)	3.10 (14)
Blackbody				1.03 (23)

*Exponents are in parentheses; units are $\text{ergs}/\text{cm}^3/\text{s}$.

Table 3.

**Calculated Power Densities for an Argon Plasma with
 $T = 30 \text{ keV}$, $n = 3 \times 10^{16} \text{ cm}^{-3}$, and $R = 100 \text{ cm}^*$.**

Model	Free-Free	Bound-Free	Bound-Bound	Total
CRE with Photoabsorption	4.40 (11)	1.37 (12)	3.29 (12)	5.10 (12)
LTE	6.96 (11)	5.46 (12)	4.20 (12)	1.04 (13)
CRE without Photoabsorption	4.22 (11)	1.24 (12)	5.06 (11)	2.17 (12)
Optically Thin	4.24 (11)	1.28 (12)	3.09 (14)	3.10 (14)
Blackbody				2.50 (16)

*Exponents are in parentheses; units are $\text{ergs/cm}^3/\text{s}$.

Table 4.

**Calculated Power Densities for an Argon Plasma with
 $T = 2 \text{ keV}$, $n = 3 \times 10^{16} \text{ cm}^{-3}$, and $R = 400 \text{ cm}^*$.**

Model	Free-Free	Bound-Free	Bound-Bound	Total
CRE with Photoabsorption	2.26 (8)	1.36 (9)	1.17 (7)	1.60 (9)
LTE	7.81 (8)	7.34 (9)	2.07 (7)	8.14 (9)
CRE without Photoabsorption	2.22 (8)	6.13 (8)	7.33 (6)	8.42 (8)
Optically Thin	2.42 (8)	2.95 (9)	6.15 (9)	9.34 (9)
Blackbody				1.24 (11)

*Exponents are in parentheses; units are $\text{ergs/cm}^3/\text{s}$.